Slab Dehydration and Mantle Upwelling in the Vicinity of the Sumatra Subduction Zone: Evidence from Receiver Function Imaging of Mantle Transition Zone Discontinuities

Fansheng Kong[1,2] , **Stephen S. Gao[2]** , **Kelly H. Liu[2]** , **Weiwei Ding[1]** , and **Jiabiao Li[1]**

[1]Key Laboratory of Submarine Geosciences, Second Institute of Oceanography, Ministry of Natural Resources, Hangzhou, China, [2]Geology and Geophysics Program, Missouri University of Science and Technology, Rolla, MO, USA

Abstract   A total of 10,586 *P*-to-*S* radial receiver functions recorded by 64 broadband seismic stations were utilized to image the 410 and 660 km discontinuities (d410 and d660, respectively) bordering the mantle transition zone (MTZ) beneath the Sumatra Island, the Malay Peninsula, and the western margin of the South China Sea. The d410 and d660 were imaged by stacking receiver functions in successive circular bins with a radius of 1°, after moveout corrections based on the 1-D IASP91 Earth model. The resulting apparent depths of the discontinuities exhibit significant and spatially systematic variations. The apparent depths of the d410 and d660 range from 382 to 459 km and 637 to 700 km with an average of 406 ± 13 and 670 ± 12 km, respectively, while the corresponding values for the MTZ thickness are 217 to 295 km and 261 ± 13 km. Underneath southern Sumatra and adjacent regions, the MTZ is characterized by an uplifted d410 and a depressed d660. While the former is probably caused by the low temperature anomaly, the latter is most likely related to a combination of the low temperature anomaly and dehydration associated with the subducted Australian Plate that has reached at least the d660. In contrast, an abnormally thin MTZ is imaged to the southwest of the Toba Caldera. This observation, when combined with results from previous seismic tomography studies, can be explained by advective thermal upwelling through a slab window.

1. Introduction

The subduction of the Australian Plate beneath the Sunda Plate along the Sumatran Trench (Figure 1) has resulted in numerous active volcanoes along the western margin of the Sumatra Island, as well as devastating earthquakes including the 26 December 2004 Mw 9.1–9.3 mega-earthquake (Stein & Okal, 2005). The subduction is also responsible for the formation of the Toba supervolcano, which is home to the largest terrestrial Quaternary caldera in the world (Chesner & Luhr, 2010). The most recent eruption of the supervolcano took place ~74,000 years ago (Chesner et al., 1991) and is believed to have had a significant impact on the biosphere of the whole Earth (e.g., Chesner & Luhr, 2010; Rampino & Self, 1992).

Global Positioning System measurements (Simons et al., 2007) and absolute plate motion modeling (Argus et al., 2011) reveal significant convergence between the Australian and Sunda plates with a subduction rate of ~64 mm/yr at a direction of 40° clockwise from north (Figure 1). The subducting Australian Plate is composed of plate segments with different ages, separated by the Investigator Fracture Zone (IFZ), a 2,500 km long transform zone composed of several subridges (Figure 1) (Koulakov et al., 2016; Lange et al., 2010). In the mapped area of Figure 1, the youngest oceanfloor is about 46 Main age along an NE-SW oriented zone and becomes older away from this zone. The oceanfloor age increases suddenly by about 10 Ma across the easternmost branch of the IFZ (Muller et al., 1997).

To better comprehend the relationship between slab subduction and the dynamic processes observed on the surface, a number of seismic tomography studies have been conducted in Sumatra and surrounding areas (e.g., Amaru, 2007; Hall & Spakman, 2015; Huang et al., 2015; Li et al., 2008, 2018; Liu et al., 2018; Obayashi et al., 2013; Pesicek et al., 2010). Most of the resulting tomographic images reveal the presence of high velocity anomalies associated with the subduction of the relatively cold Australian Plate, but significant discrepancies exist among previous studies regarding the depth extent, geometry, and integrity of the subducted slab segments (Figure 2). Some studies advocate that the subducted slab segments beneath
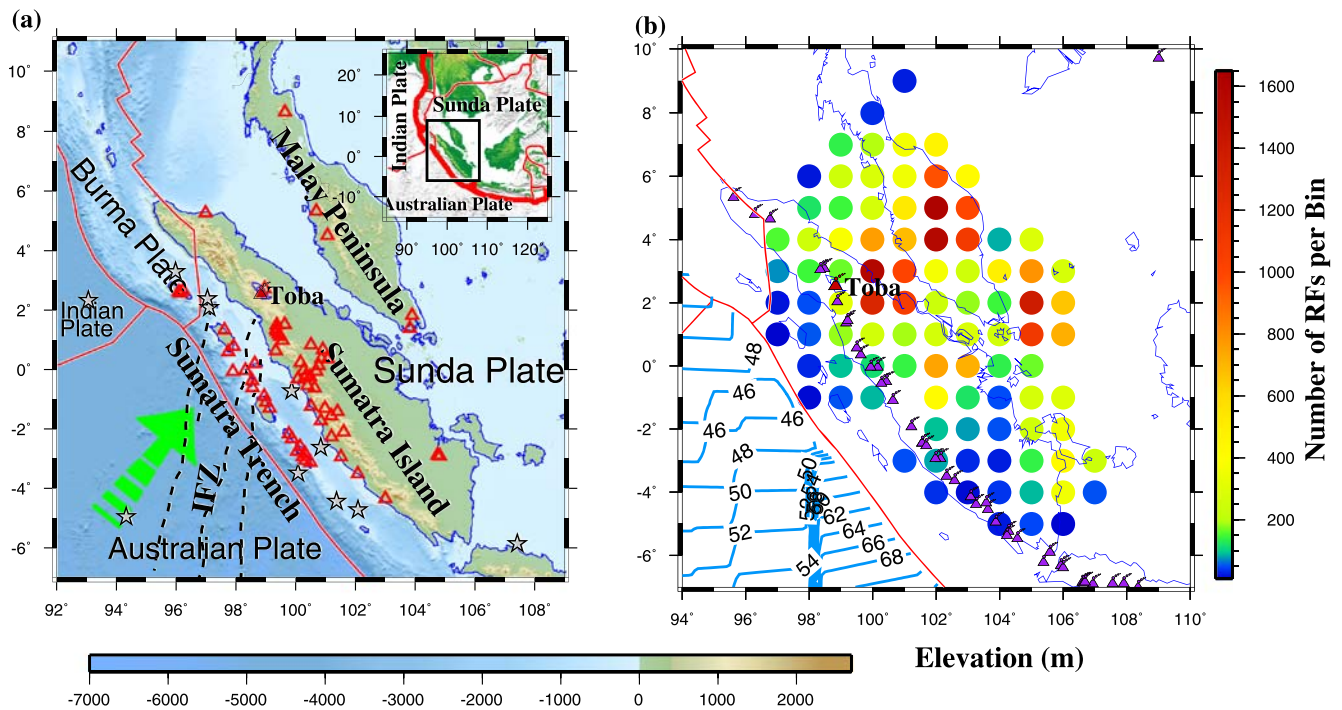
Figure 1. (a) Topographic relief map of the study area showing the broadband seismic stations used in the study (triangles). The stars show the epicenters of the earthquakes with magnitude ≥7.5 since 2000. The green arrow shows the movement direction of the Australian Plate relative to the Sunda Plate based on the NNR-MOREVEL56 model (Argus et al., 2011). The inset map shows the study area in black rectangle with solid red lines denoting the major tectonic boundaries. IFZ: Investigator Fracture Zone. (b) Filled circles showing the center of bins that have a radius of 1°, with colors representing the number of RFs per bin. The purple volcano symbols represent Cenozoic volcanoes, and the red symbol denotes the location of the Toba Caldera. The blue contour lines show oceanfloor ages in million years.

Sumatra and adjacent regions have penetrated into the lower mantle (e.g., Huang et al., 2015; Li et al., 2008; Liu et al., 2018; Lu et al., 2019; Pesicek et al., 2010) (Figure 2), while others suggest high velocity anomalies mainly concentrated above the bottom or top of the mantle transition zone (MTZ) (e.g., Amaru, 2007; Li et al., 2018). Additionally, the magnitude of the anomalies differs greatly among the previous studies, especially for the MTZ and the uppermost lower mantle (Figure 2).

Another enigmatic issue among previous studies is the presence or absence of a slab window beneath northern Sumatra, approximately directly underneath the Toba Caldera. Studies that have suggested the existence of such a window indicate that the Earth-surface-projected location is above the prolongation of the IFZ (e.g., Hall & Spakman, 2015; Koulakov et al., 2016; Liu et al., 2018; Page et al., 1979). Seismic imaging reveals significant amounts of melted material in the crust beneath the Toba Caldera (e.g., Jaxybulatov et al., 2014), probably as a consequence of the upward migration of volatiles associated with the IFZ and the slab window in the mantle wedge (Koulakov et al., 2016). While most of the studies that find lower-than-normal upper mantle velocities above the slab window extending to the Toba Caldera hypothesize the extensive magmatism as the consequence of mantle upwelling through the slab window, there is a general lack of convincing evidence to support such an upwelling (e.g., Koulakov et al., 2016; Liu et al., 2018). The discrepancies among seismic tomographic images can be attributed to a combination of the inadequate raypath coverage in the study area, different tomographic inversion techniques, different parameters used in the inversions, and the limited spatial resolution of the tomographic inversion techniques especially at the MTZ depth (Foulger et al., 2014, 2015).

As demonstrated by numerous previous mineral physics and seismological investigations, the existence and depth extent of subducted slabs as well as the upwelling of high temperature mantle materials through slab windows can be reliably constrained by the depth variations of the 410 and 660 km discontinuities (d410 and d660, respectively) (e.g., Anderson, 1967; Collier et al., 2001; Dahm et al., 2017; Shearer & Masters, 1992; Yu et al., 2017). The d410 and d660 are well established in all modern global velocity models, with a mean depth of 410 km for the d410 and 660 km for the d660, and a mean thickness of 250 km
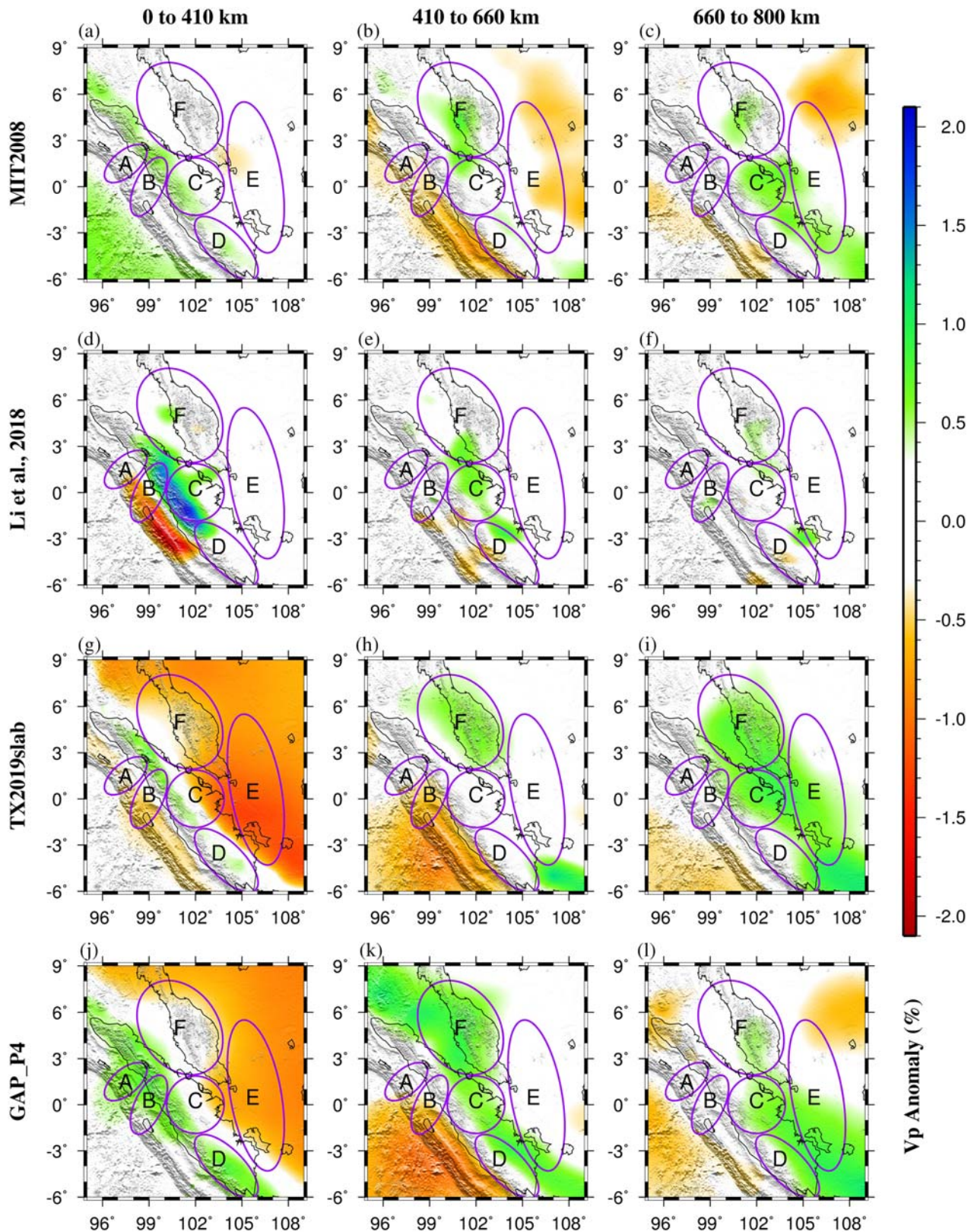
Figure 2. Averaged upper mantle (0–410 km; left column), MTZ (410–660 km; middle column), and topmost lower mantle (660–800 km; right column) *P*-wave velocity anomalies from previous studies. MIT2008, TX2019slab, and GAP_P4 are from Li et al. (2008), Lu et al. (2019), and Obayashi et al. (2013), respectively. The reference model of the first three models is AK135 (Kennett et al., 1995) and that for the fourth one is GAP_P2. The ellipses mark the six regions with similar characteristics in the resulting discontinuity depths.

for the MTZ (Kennett & Engdahl, 1991). The MTZ discontinuities are associated with mineral phase transitions from α-olivine to wadsleyite at the d410 (Ringwood, 1975), and from ringwoodite to bridgmanite at the d660 (Ito & Katsura, 1989; Yamazaki & Karato, 2001). There is also a phase transition from wadsleyite to ringwoodite at ~520 km, which is not observed globally. The phase transitions are closely related to temperature and pressure, satisfying a relationship defined by the Clapeyron slope (Bina & Helffrich, 1994; Fei et al., 2004; Helffrich, 2000). Phase transitions across the d410 and d660 have a positive and negative Clapeyron slope, respectively. Consequently, for a colder MTZ, an uplifted d410 and a depressed d660 are expected, resulting in a thicker MTZ, while a depressed d410 and an uplifted d660 with a thinner than normal MTZ are expected for an MTZ region with positive temperature anomalies (Helffrich, 2000; Ito & Katsura, 1989; Ringwood, 1975). If a temperature higher than 1800°C (which is approximately 200°C above the global average) is present at the d660, the phase transition across the d660 would be from majorite to perovskite, which has a positive Clapeyron slope of 1.0 MPa/K (Hirose, 2002).

In addition to thermal anomalies, another factor that may contribute to the undulation of MTZ discontinuities is the presence of an anomalously large amount of water in the MTZ. Previous experimental studies (Litasov et al., 2005; Ohtani & Litasov, 2006; Smyth & Frost, 2002) suggest that the effect of water on the topography of the d410 and d660 is similar to that of negative temperature anomaly, that is, leading to an uplifted d410 and a depressed d660. Water can also broaden the phase transition related to the d410, making the discontinuity more difficult to observe seismically due to the reduced sharpness of the discontinuity (Smyth & Frost, 2002). Besides its influence on the phase transitions, a recent study (Wang et al., 2018) has demonstrated that hydration of olivine and its high-pressure polymorphs (e.g., wadsleyite and ringwoodite) can modify their densities, bulk modulus, and shear modulus, causing P-wave negative velocity anomalies up to approximately −3.35% in a water saturated MTZ under the assumption of a pyrolite composition model. The water effects on the elastic properties of olivine and its high-pressure polymorphs, however, are still debated as there is a lack of experimental constraints at temperatures expected at MTZ pressures (Schulze et al., 2018; Thio et al., 2016).

The most recent regional-scale study of MTZ discontinuities using receiver functions (RFs) in the vicinity of the Sumatra subduction zone was conducted by Saita et al. (2002), which utilized broadband seismic data recorded by 23 stations, among which six were located in the investigated area of this study (Figure 1). The results exhibit significant depth variations of the d410 and d660 by up to 40 km relative to the corresponding values in the IASP91 Earth model (Kennett & Engdahl, 1991). The depth undulations are explained as the consequence of subducted slabs beneath Sumatra and adjacent regions (Saita et al., 2002).

This study aims at investigating the topography of the MTZ discontinuities beneath the Sumatra Island, Malay Peninsula, and the westernmost portion of the South China Sea, by taking the advantage of a more than 10-fold increase in the number of broadband seismic stations over the most recent MTZ study using RFs (Saita et al., 2002). Most of the stations were deployed in response to the aftermath of the 2004 mega-earthquake. The resulting discontinuity depths and MTZ thickness provide new constraints on the depth extent of the subducted slabs, thermal interactions between the subducted slab and the ambient mantle, slab dehydration, and upwelling of hot mantle materials from the top of the MTZ through the slab window with an unprecedented spatial resolution.

2. Data and Methods

The broadband passive seismic data used in the study were recorded by 64 stations over the 25-year period from April 1993 to September 2018. Data from 58 of the stations were obtained from the Incorporated Research Institutions for Seismology (IRIS) Data Management Center (DMC), and those from the other six stations were from the GEOFON data centre of the GFZ German Research Centre for Geosciences. The seismic data set was requested based on the following criteria: (1) the epicentral distances range from 30° to 100°; (2) stations are located in the area of −6°N to 9°N and 95°E to 108°E; (3) the cutoff magnitude (M_c) is a function of the epicentral distance (Δ) and focal depth (D), expressed as $M_c = Mw_{min} + (\Delta - \Delta_{min})/(180.0 - \Delta_{min}) - D/D_{max}$, where $Mw_{min} = 5.2$, $\Delta_{min} = 30°$ and $D_{max} = 700$ km. This equation was initially designed to balance the quantity and quality of the seismic data to be requested (Liu & Gao, 2010) and has been utilized in a number of previous studies (e.g., Dahm et al., 2017; Gao & Liu, 2014b; Sun et al., 2018, 2020; Yu et al., 2017). In this equation, the epicentral distance and the focal depth are normalized by the corresponding maximum values. The data processing procedure and parameters are the same as those used in
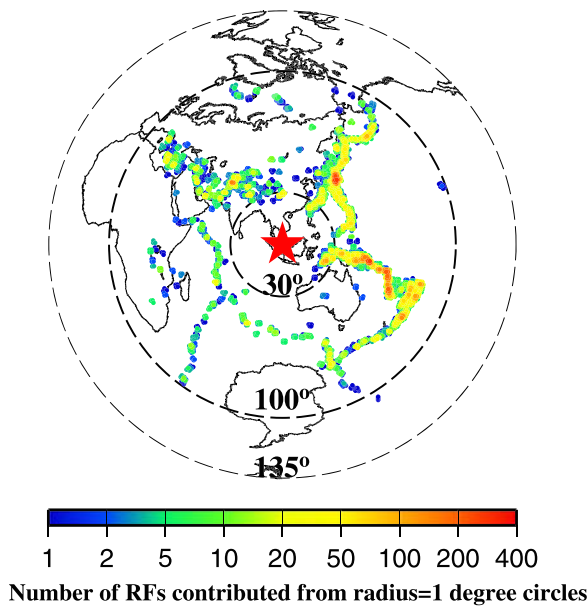
Figure 3. An azimuthal equidistant projection map centered at the study area showing the distribution of earthquakes utilized in the study. Each circle represents a circular area with a radius = 1°. The color of the circles represents the number of RFs from earthquakes that are located in the circles.

Gao & Liu (2014a, 2014b) and are briefly described below. To enhance the signal-to-noise ratio (SNR) of the seismograms, we applied a four-pole, two-pass bandpass Bessel filter with corner frequencies of 0.02 and 0.2 Hz. Before the deconvolution process for obtaining the RFs, we applied two SNR based procedures to select high-quality RFs (Gao & Liu, 2014a) and rejected seismograms with a P-wave SNR on the vertical component less than 4.0. The SNR is defined as $\max|A_s|/|\bar{A}_n|$, where $\max|A_s|$ is the maximum absolute amplitude on the vertical component in the time window of 8 s before and 12 s after the predicted arrival time of the first P-wave calculated using the IASP91 Earth model, and $|\bar{A}_n|$ is the mean of the absolute amplitude of the waveform 10–20 s before the predicted P-wave arrival (Gao & Liu, 2014b).

The portion of the seismograms in the time window of 20 s before and 260 s after the first arrival was utilized to compute radial RFs using a deconvolution procedure in the frequency-domain with a water level of 0.03 (Ammon, 1991; Clayton & Wiggins, 1976). We tested the influence of the water level on the RFs by using several water level values ranging from 0.001 to 0.11. As demonstrated in Figure S1 in the supporting information, no significant difference in the resulting RFs can be observed for water level values between 0.01 and 0.07. To reduce the degenerating effects of the strong PP arrivals to the resulting RFs, a set of exponential weighting functions with a half width of 30 s centered at the theoretical arrival time of the PP were applied to the seismograms prior to the RF computation (Gao & Liu, 2014a). The RFs were visually verified to remove those with abnormally large arrivals (relative to the first P arrival) in the pre-P window and P-wave coda. A total of 10,586 high-quality RFs from 3,685 events (Figure 3) recorded by 64 stations (Figure 1) were used for the study.
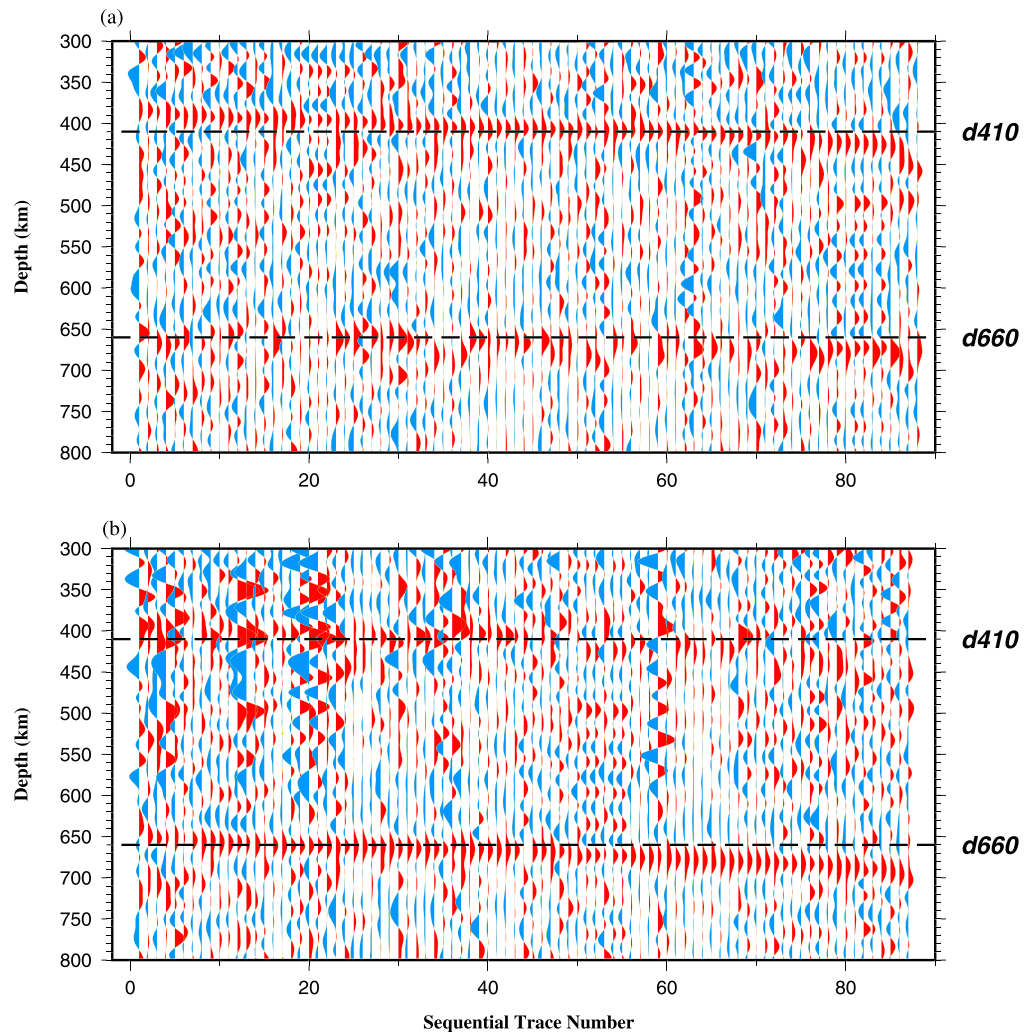
The RFs were grouped into radius = 1° circular bins based on the theoretical coordinates of P-to-S converted phase (P_ds) at the middle of the MTZ (i.e., 535 km). The distance between the centers of neighboring bins is 1 geographic degree. An alternate approach is to group the RFs based on the piercing point locations for each of the candidate depths of possible discontinuities (e.g., Dueker & Sheehan, 1998; Liu et al., 2003). As discussed in the next section, the resulting discontinuity depths and MTZ thickness measurements are statistically identical from both ray-piercing point grouping approaches.

RFs in the same bins were then moveout corrected using the IASP91 Earth model under the nonplane wavefront assumption and were stacked if the number of RFs in a bin is 12 or greater to form depth series for the range of 350–750 km, with a vertical interval of 1 km. The number of traces participated in the stacking for each bin ranges from 12 to 1,619 (Figure 1). Due to the nonplane nature of the wavefront of the teleseismic P-wave, the ray parameters of the direct P-wave and the P_ds phase generated from the MTZ discontinuities are not exactly the same, leading to an error of a few kilometers in the resulting depths if they are considered to be the same (Gao & Liu, 2014a). The magnitude of the error increases with increasing ray parameters, leading to incoherent stacking and thus reduced stacking amplitude and broadening of the P_ds pulses associated with the d410 and d660 arrivals (Gao & Liu, 2014a, 2014b). Therefore, the nonplane wave approach, which takes the difference in the ray parameter between the direct P and the P_ds waves into consideration, can result in more sharply focused P_ds arrivals and more accurately determined depths than the plane wave approach which assumes identical ray parameters between the direct P and P_ds phases.

For each bin, a bootstrap resampling procedure with 50 iterations (Efron & Tibshirani, 1986; Liu et al., 2003) was utilized to calculate the mean and standard deviation of the resulting depths of the MTZ discontinuities as well as the MTZ thickness. For each bootstrap iteration, the depths of the d410 and d660 were determined by picking the maximum stacking amplitude in a predefined depth window, which ranges from 380 to 440 km for the d410, and from 630 to 690 km for the d660, on the resulting depth series. Then the automatically determined depths were visually examined, and the predefined depth window is adjusted if necessary to include P_ds from the target discontinuity. For the majority of the time series, the P_ds phase from the d410 and d660 are clearly observed, especially when the traces are plotted sequentially based on the determined
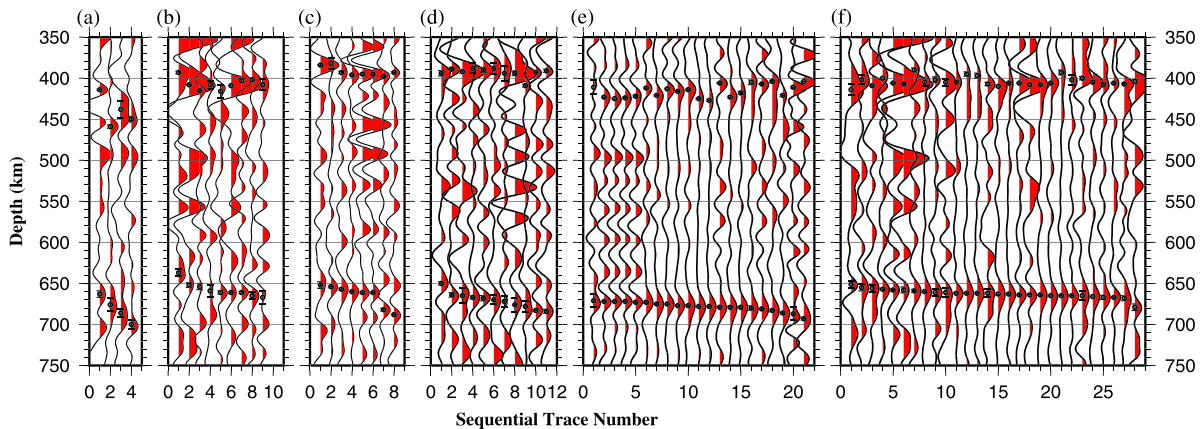
Figure 4. (a) Depth series in 1° radius bins plotted with respect to the sequentially increasing depth of the d410. (b) Same as Figure 4a but for sequentially increasing depth of the d660. To make the arrivals associated with the d410 and d660 more observable, the arrivals were normalized using the maximum value between 380 and 480 km and 630 and 750 km, respectively.

depths of the discontinuities (Figure 4) or when they are grouped based on geographic regions (Figure 5). For a small portion of the traces that have multiple arrivals with comparable amplitudes, the depth window was adjusted so that the arrival with a shape and depth that are similar to those of the nearby bins was selected. To confirm the reliability of the resulting depth measurements, we produced a vespagram for each of the six regions (Figure 2), using a reference slowness of 6.5 s/° (Figure 6). The resulting depth series (Figure 5) and the vespagrams (Figure 6) suggest that P-to-S conversions from the d410 and d660 can be reliably identified on the vast majority of the bins for all the regions, with the exception of the d660 from Region B where ambiguities remain on some of the traces due to low amplitudes of the P_ds from the d660. Fortunately, as demonstrated below, this arrival plays an insignificant role in reaching the main conclusions of the study.

3. Results

3.1. Apparent Depths

Totally 88 bins with reliable depth measurements of the d410 were obtained. The number is 87 for the d660 and 81 for the bins that possess clear arrivals for both the d410 and d660 (Table S1). The observed d410 depths for the study area range from 382 to 459 km with a mean value of 406.3 ± 13.2 km, and they are 637 to 700 km and 669.5 ± 11.7 km for the d660, respectively. The observed MTZ thickness ranges from 217 to

Figure 5. (a–f) Mean depth series (red wiggles) with both the d410 and d660 depth measurements obtained by stacking RFs after normal moveout corrections in 1° radius bins, plotted with respect to the sequentially increasing depth of the d660 for Regions A–F, respectively. The traces were normalized by the maximum amplitude in the depth range of 620–720 km. The solid dots with vertical bar represent the determined depths of the MTZ discontinuities and the SD. Note that the multiple arrivals on the left-most trace in Region A might be caused by the fact that the bin is near the margin between Regions A and B, and thus samples discontinuities from both regions.

295 km, with a mean value of 261.2 ± 13.3 km, which is 11.2 km thicker than the global average of 250 km in the IASP91 Earth model. The results are statistically comparable to those calculated using RFs grouped at 410 km (Figure S2) and 660 km (Figure S3), which lead to a mean MTZ thickness of 259.9 ± 14.6 km.

Figure 7 shows the spatially continuous MTZ discontinuity depths and MTZ thickness, which were obtained by using a continuous curvature surface griding algorithm with a tension factor of 0.5 (Smith & Wessel, 1990). Since the 1-D IASP91 Earth model is utilized to produce the results, the resulting depths of the d410 and d660 are apparent rather than true depths and are functions of temperature anomalies around the d410 and d660, the existence of anomalously hydrated minerals in the MTZ, and velocity anomalies above the discontinuities. Since velocity anomalies in the crust and upper mantle influence both the apparent depths of the d410 and d660 almost equally, a high cross-correlation coefficient (XCC) between the d410 and d660 depths is expected if the true depths of the d410 and d660 vary insignificantly over the study area. High velocity anomalies in the crust and upper mantle lead to apparent uplifts of both the d410 and d660, while low velocity anomalies correspond to apparent depressions for both discontinuities. A high XCC between the d410 and d660 depths can also be caused by the presence of very significant positive thermal anomalies
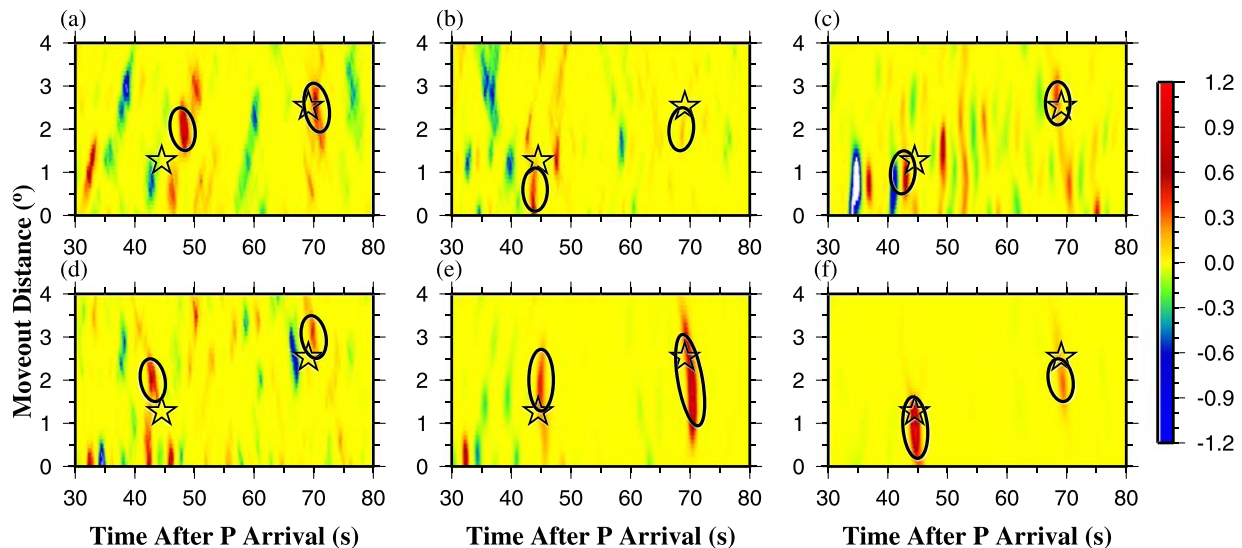
Figure 6. (a–f) Fourth-root stacking results for a reference slowness of 6.5 s/° using RFs from the bins in Regions A–F, respectively. The stars represent the predicted locations of the $P_{410}s$ and $P_{660}s$, and the ellipses mark the observed arrivals.
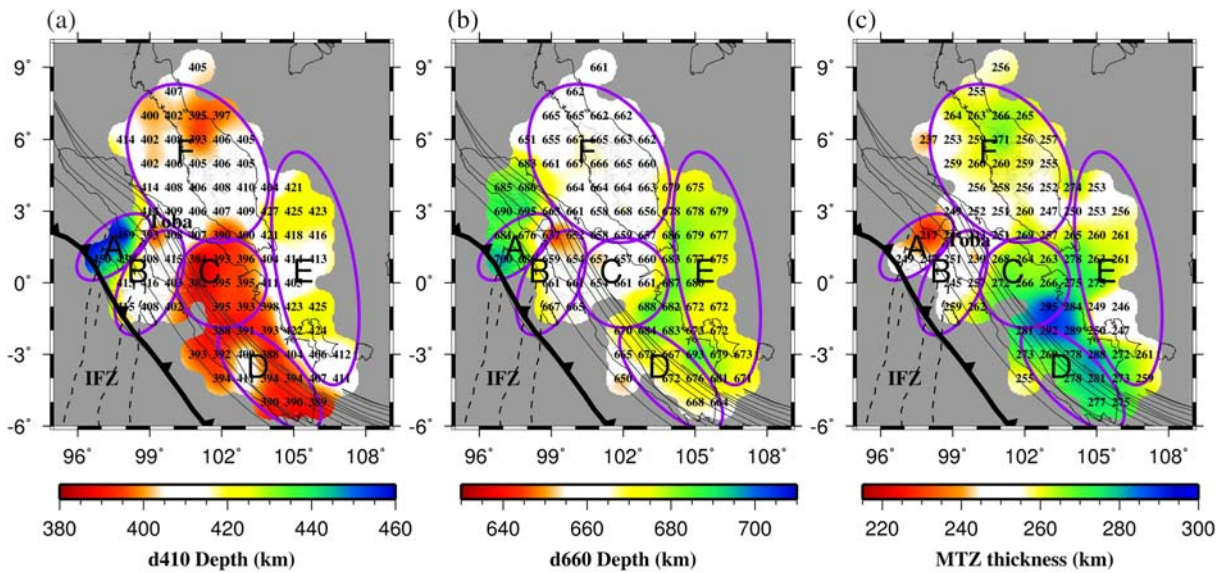
Figure 7. (a) Spatial distribution of apparent depths of the d410. (b) Same as (a) but for the d660. (c) MTZ thickness measurements. Black lines represent the depth contours of the subducted slab from Gudmundsson and Sambridge (1998). Please note that only the bins that have both the d410 and d660 depth measurements can result in a MTZ thickness measurement, which are shown in (c).

in the vicinity of the discontinuities when the temperature is higher than 1800°C around the d660, which causes positive Clapeyron slopes for both the d410 (Bina & Helffrich, 1994) and d660 (Hirose, 2002), and consequently leads to a positive XCC. Such a high temperature situation, however, may not be relevant in the study area as it is dominated by slab subduction. The XCC between the observed apparent depths of the d410 and d660 in the study is 0.41 (Figure 8). In comparison, for the contiguous United States, this value is as large as 0.84 (Gao & Liu, 2014b), and for the Arabian Plate and adjacent areas, it is 0.81 (Mohamed et al., 2014). The moderate XCC for the study area suggests that a significant portion of the observed spatial variation of the apparent depths comes from thermal, water content, or velocity anomalies in the MTZ.

Based on the characteristics of the observed discontinuity depths and MTZ thickness, we divided the study area into six regions (Figures 2 and 7 and Table 1). In the area west of the Toba Caldera (Region A), both the d410 and d660 are apparently depressed, with the former possessing a greater magnitude of about 9 km. Further south (Region B), the d410 and the less well defined d660 are found to have normal values. The largest apparent uplift of about 18 km of the d410 was revealed in central Sumatra (Region C), wherein the d660 depresses by about 4 km, leading to an MTZ that is about 22 km thicker on average. For southern Sumatra (Region D), the d410 is 16 km shallower and the d660 is 11 km deeper than normal, and the resulting MTZ thickness is 28 ± 3 km thicker than normal, a value that is the largest in the entire study area. The d410 observed in the South China Sea portion of the Sunda Plate (Region E) is about 6 km deeper than the normal depth, and the d660 is about 18 km deeper than normal. In contrast to the significant depth variations of the d410 and d660 beneath Sumatra, most of the Malay Peninsula (Area F) exhibits a slightly uplifted d410 and a marginally depressed d660 with an MTZ that is about 8 km thicker than the global average.

3.2. Velocity-Corrected Depths

We next convert the apparent depths into "true" depths using a number of global-scale tomographic models, by applying the following velocity correction procedure, whose details can be found in Gao and Liu (2014b). In this study, we use three global *P*-wave velocity models, including Li et al. (2008), Lu et al. (2019), and Obayashi et al. (2013) (Figure 2), which are referred to as MIT2008, TX2019slab, and GAP_P4, respectively, a global model for both *P*- and *S*-waves (Lu et al., 2019), and a regional *P*-wave model (Huang et al., 2015) for velocity corrections. The corrections were carried out by interpolating the velocity anomalies into layers with a thickness of 10 km for the depth range of 0 to 700 km. For models with only *P*-wave velocities, the shear wave velocity anomaly for each layer is calculated using the *P*-wave velocity anomaly and an optimal value of γ, which is defined as $\gamma = dln(V_s)/dln(V_p)$. The optimal value is determined separately for each of the *P*-wave models and is obtained by searching for the γ value that corresponds to the minimum XCC value between the corrected d410 and d660 depths (Gao & Liu, 2014b).
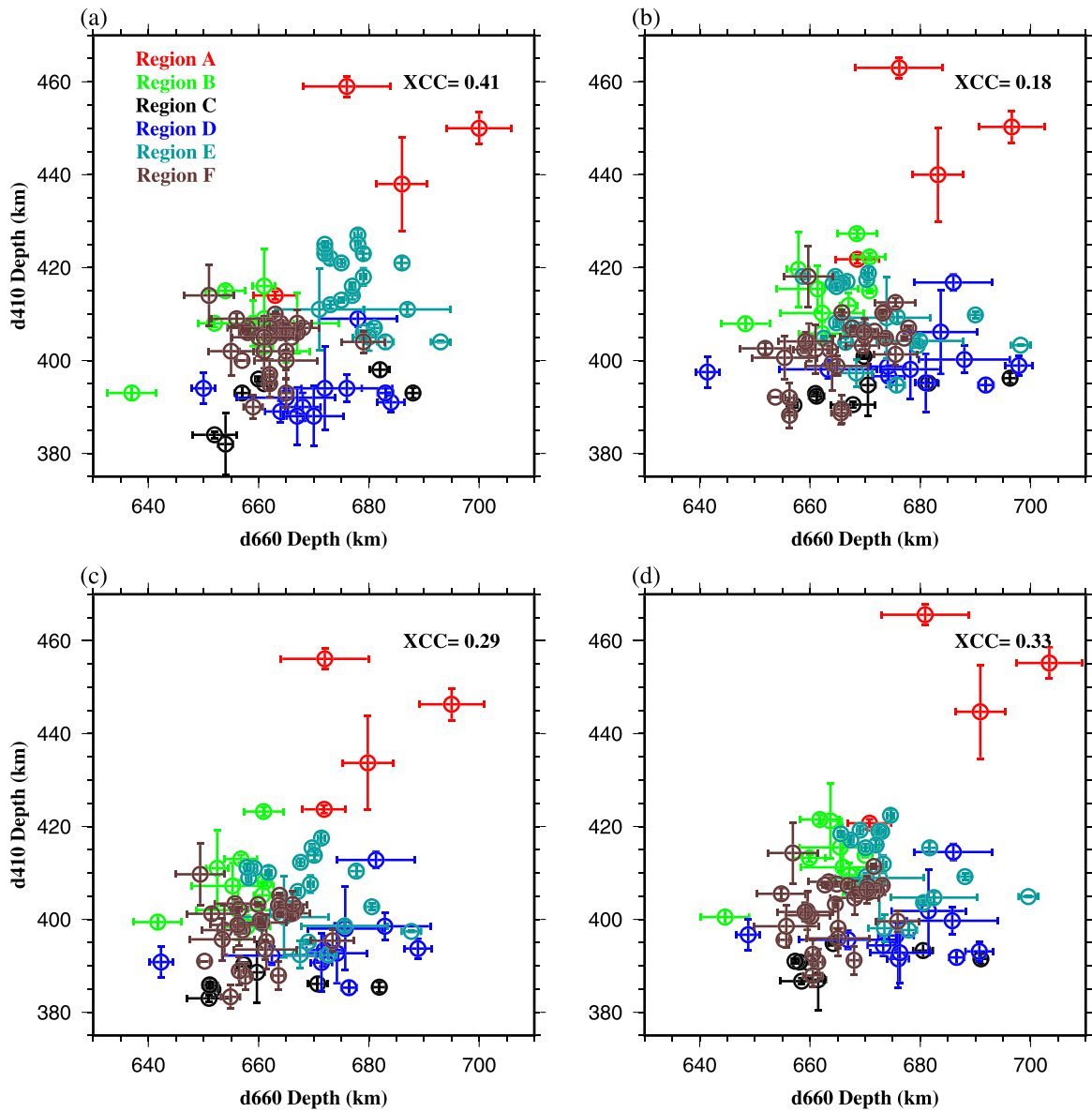
Figure 8. (a) Apparent depths of the d410 plotted against the apparent d660 depths. (b–d) Same as (a) but for the corrected depth measurements using MIT2008, TX2019slab, and GAP_P4, respectively. The regions which the measurements belong to are indicated by different colors. XCC: Cross-Correlation Coefficient.

Given the fact that in an olivine dominated phase transition system, both temperature and water content anomalies in the MTZ lead to opposite undulations of the d410 and d660 (Litasov et al., 2005; Ringwood, 1975), the XCC between the perfectly corrected d410 and d660 depths is close to zero (for the situation when there are no thermal and water content anomalies in the MTZ) or negative. A positive XCC indicates incomplete correction. The optimal γ values are 3.25 for MIT2008, 1.7 for TX2019slab, 1.55 for GAP_P4, and 1.7 for Huang et al. (2015). The XCC between the corrected d410 and d660 depths decreases, from 0.41 between the uncorrected depths to 0.18 for MIT2008, 0.29 for TX2019slab, 0.33 for GAP_P4, 0.35 for V_p and V_s in Lu et al. (2019), and 0.29 for Huang et al. (2015) (Figures 8,9, S3, and S4). The mean values of the resulting d410 depth, d660 depth, and MTZ thickness after the velocity corrections using MIT2008, TX2019slab, GAP_P4, V_p and V_S in Lu et al. (2019), and V_p in Huang et al. (2015) are (406.7 ± 12.6 km, 669.8 ± 11.1 km, 263.1 ± 15.3 km), (401.4 ± 12.7 km, 664.2 ± 10.4 km, 262.8 ± 13.9 km), (405.9 ± 13.9 km, 670.5 ± 11.0 km, 264.5 ± 14.6 km), (405.9 ± 12.3 km, 672.5 ± 11.7 km, 266.5 ± 13.6 km), and (407.4 ± 13.0 km, 670.7 ± 9.5 km, 263.3 ± 13.7 km), respectively.

Table 1
Mean Measurements for the Six Subregions

Region	$d410 \pm \sigma_{d410}$ (km)	$d660 \pm \sigma_{d660}$ (km)	MTZ $\pm \sigma_{MTZ}$ (km)	Number of bins	Number of RFs
A	440.3 ± 9.8	681.2 ± 6.1	241.0 ± 8.0	4	246
B	408.2 ± 2.1	657.4 ± 3.0	250.6 ± 2.7	9	2,247
C	392.3 ± 1.8	664.4 ± 4.7	272.4 ± 4.0	8	1,269
D	394.0 ± 1.9	670.6 ± 2.9	277.7 ± 3.0	11	324
E	415.8 ± 1.7	678.1 ± 1.2	262.3 ± 2.5	21	2,893
F	404.4 ± 1.0	664.9 ± 1.7	258.4 ± 1.4	28	5,890

The resulting corrected depths and especially the corrected MTZ thickness (Figures 9, S4, and S5) are similar to the corresponding apparent measurements (Figure 7). To facilitate discussions, in Figure 10, we plot the original and corrected depths for two of the regions with the largest MTZ thinning (Region A) and thickening (Region D). The similarities between the apparent and corrected depths, and the limited reduction in the XCC's after the correction suggest that the velocity corrections did not effectively remove the influence of velocity heterogeneities on the observed MTZ discontinuity depths, probably due to limited horizontal and vertical resolutions of the velocity models in this area which is poorly sampled by seismic stations. Consequently, instead of randomly selecting one of the corrected sets of measurements, in the following we mostly rely on the apparent depths to infer the velocity and thermal structures of the upper mantle and MTZ, as applied to numerous previous MTZ discontinuity studies (e.g., Dahm et al., 2017; Gao & Liu, 2014b; Lawrence & Shearer, 2006; Sun et al., 2018). As detailed below, the corrected MTZ thickness results (rather than the absolute discontinuity depths), which are almost identical to the apparent depths for all the velocity models, play the determining role in reaching the conclusions.

4. Discussion

The observed systematic spatial variations of the MTZ thickness and discontinuity depths can provide new constraints on a number of models associated with the structure and geodynamics of the Sumatra subduction zone and adjacent areas. Note that although significant differences exist among the different velocity models (e.g., Li et al., 2008, 2018; Obayashi et al., 2013), the subducted Australian Plate beneath the Sumatra subduction zone is imaged as a steep high velocity feature by most studies. Given this observation and the fact that the diameter of the circular bins is 2° (about 220 km), in the following discussions, the slab in the upper mantle and the MTZ is assumed to be subvertical when the velocity and other anomalies are estimated.

4.1. Thermal Upwelling Through a Slab Window

Above the proposed slab window (e.g., Hall & Spakman, 2015; Koulakov et al., 2016; Page et al., 1979) west of the Toba Caldera (Region A), the d410 and d660 are apparently depressed by 4–49 and 3–40 km (Figures 5 and 7), respectively, resulting in a thinner than normal MTZ for all the bins. On average, the d410 is apparently depressed by about 30 ± 10 km, and the d660 is apparently depressed by 21 ± 6 km (Table 1). Due to the greater depression of the d410, the resulting MTZ thickness in this area is about 9 ± 8 km thinner compared to the global average of 250 km.

The simplest model that can account for the observations in Region A involves a low velocity zone (LVZ) extending from the surface to the upper MTZ. A 21 km apparent depression of both the d410 and d660 would require a V_p anomaly of −1.5% relative to the IASP91 Earth model in the upper mantle. If we assume that this LVZ extends to the d410 without reducing the magnitude, the estimated temperature anomaly near the d410 is about +255 K, if the scaling relationship of $dV_p/dT = -4.8 \times 10^{-4}\,\mathrm{km\,s^{-1}\,K^{-1}}$ (Deal et al., 1999) is used. The increased temperature would introduce a further depression of about 20 km for the d410 for a Clapeyron slope of +2.9 MPa/K (Bina & Helffrich, 1994). The depression is about 28 km for a Clapeyron slope of +4.0 MPa/K (Katsura et al., 2004), and 13 km for a Clapeyron slope of +1.8 MPa/K (Akaogi et al., 1989). The resulting total depression would be 41, 49, and 34 km, respectively, which are all deeper than the observed 30 km for the d410. In order to fit the observed amount of depression, a model involving velocity
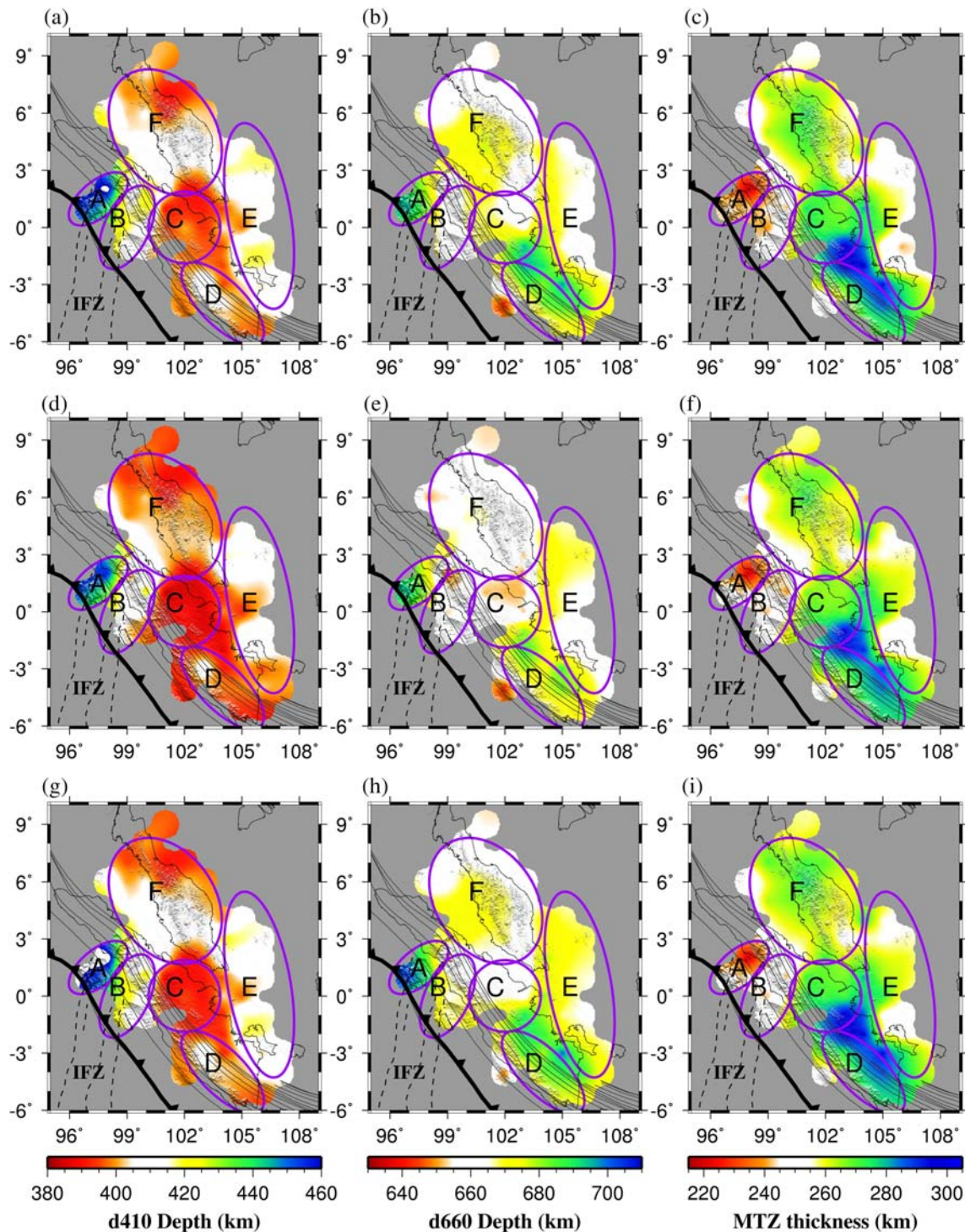
Figure 9. Corrected d410 depth, d660 depth, and MTZ thickness measurements using MIT2008 (a–c), TX2019slab (d–f), and GAP_P4 (g–i).

(and corresponding temperature) anomalies that decrease with depth is needed (Liu et al., 2018). We estimated that additional V_p anomalies ranging from -0.75% to -1.5% are needed in order to fully correct the apparent depths.

An alternate model for the observed apparent depression of both the d410 and d660 beneath Region A is that the phase transition across the d660 is from majorite to perovskite, which becomes dominant when the ambient temperature in the lower MTZ is $\sim$200°C higher than normal and is characterized by a positive
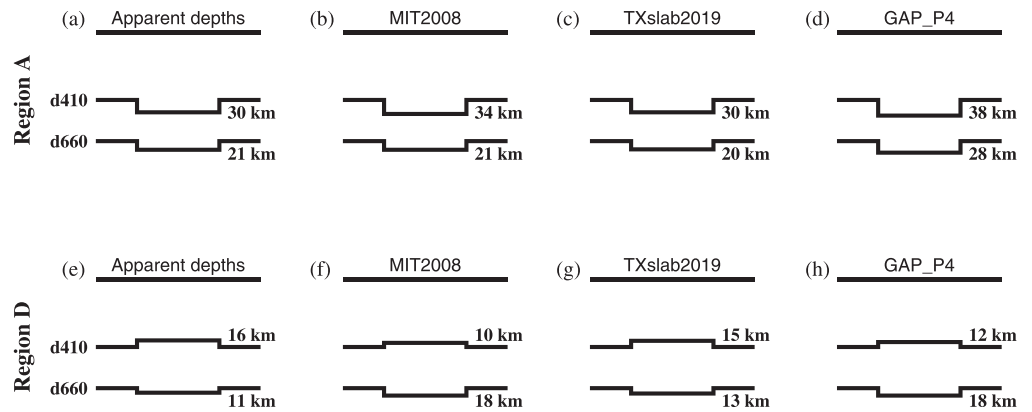
Figure 10. Resulting mean apparent d410 and d660 depths in Regions A (a) and D (e). (b,f) Same as (a,e) but for the corrected depths using MIT2008. (c,g) Same as (a,e) but using TX2019slab. (d,h) Same as (a,e) but using GAP_P4. Note that the amplitudes of the MTZ discontinuity undulations are exaggerated by a factor of 2.5.

Clapeyron slope of 1.0 MPa/K (Hirose, 2002). Using the scaling relationship between V_p and temperature anomalies (Deal et al., 1999), a V_p anomaly of about −1.1% is needed in the MTZ. Such a large anomaly in the MTZ should have been observed by the tomographic investigations (Figure 2), which all suggest negligible anomalies in the MTZ (middle column of Figure 2). Therefore, our observations are more consistent with the absence of anomalously high temperatures in the lower MTZ and the presence of upwelling of high temperature material through a slab window that only involves the upper MTZ and upper mantle.

The model is consistent with MTZ observations above slab windows in other areas such as Alaska (Dahm et al., 2017) and the Indochina Peninsula (Yu et al., 2017). Advective upwelling of hot material through the slab window can lead to reduced velocities in the upper mantle, and at the same time depress the d410 due to the higher temperature relative to the ambient mantle in the upper-most MTZ. The slab window in the study area, whose presence is also suggested by a recent seismic anisotropy study based on shear wave splitting analysis (Kong et al., 2020), is probably associated with the IFZ and linked with the feeder system of the Toba supervolcano (Koulakov et al., 2016; Liu et al., 2018).

4.2. A Hydrous Lower MTZ Beneath Southern Sumatra

One of the major features in the observed apparent MTZ discontinuity depths is the trench-parallel zone with large apparent uplifts of the d410 and smaller apparent depressions of the d660 in southern Sumatra (Regions C and D in Figure 7). In the following, we attempt to explore different scenarios that may lead to the observed apparent undulation of the discontinuities. In this section, we use the observed values for Region D, in which the observed d410 and d660 depths and MTZ thickness depart from the normal values by −16, 11, and 28 km (Table 1), respectively, for quantitative discussions of several models regarding the velocity, thermal, and water content anomalies in the upper mantle and MTZ.

4.2.1. Subduction of Anhydrous Slab Segments

This model attributes the observed depth variations to the negative temperature as well as the positive velocity anomalies associated with the subducted slabs. Under this model (Figure 11a), the observed 16 km total uplift of the d410 is the combination of two factors. The first is positive velocity anomalies above the d410. If we assume a mean V_p anomaly of 0.5% in the upper mantle (Huang et al., 2015) and a $\mathrm{dln}(V_s)/\mathrm{dln}(V_p)$ value of 2.0 (Gao & Liu, 2014b), the apparent uplift of the d410 due to upper mantle velocity anomalies alone is about 6 km. The remaining 10 km uplift of the d410 requires a temperature anomaly of about −120 K, if a Clapeyron slope of +2.9 MPa/K is applied (Bina & Helffrich, 1994).

While this model (Figure 11a) can explain the observed depths of the d410, it cannot reasonably account for the observations for the d660. Under the assumption that this negative temperature anomaly persists at the d660 depth, the resulting temperature-related depression of the d660 is merely 4 km for a Clapeyron slope of −1.3 MPa/K (Fei et al., 2004). This temperature-related depression and the 6 km apparent uplift of the d660 associated with the positive upper mantle velocity anomaly result in a 2 km apparent uplift of the d660 (Figure 11a), which is greatly different from the 11 km depression observed in this area. After correcting for the influence of upper mantle velocity anomalies on the observed d660 depth, the actual depression of the
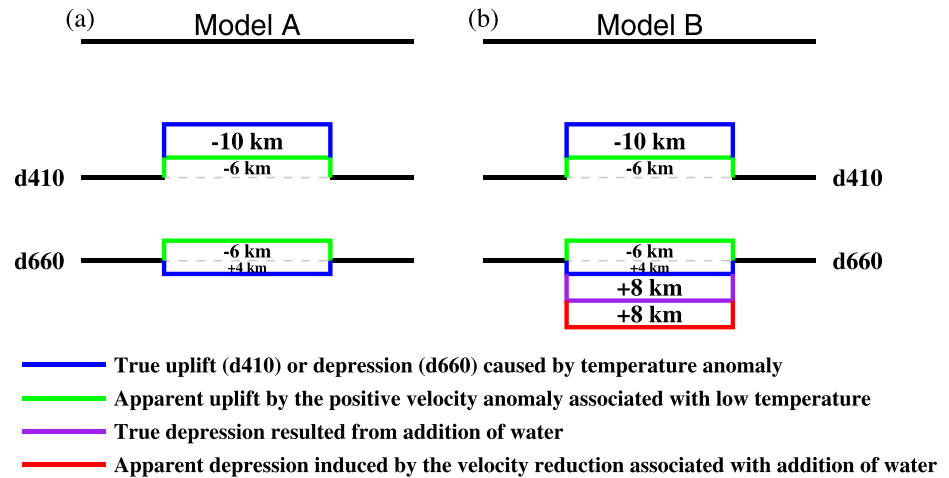
Figure 11. Schematic diagrams to explain the observed apparent MTZ discontinuity depths for (a) an anhydrous MTZ and (b) a hydrous MTZ. Positive values mean depression, and negative values denote uplift. Note that the amplitudes of the MTZ discontinuity undulations are exaggerated by a factor of 10.

d660 is 17 km resulting from combining the observed 11 km apparent depression (Table 1) and the additional 6 km from correcting the effect of upper mantle velocity anomalies. The required temperature anomaly for a 17 km depression of the d660 is about −470 K calculated using a Clapeyron slope of −1.3 MPa/K, which is approximately a fourfold increase over the magnitude of the thermal anomaly required for the observed uplift of the d410. Under the assumption that age distribution and sinking velocity play dominant roles in controlling the thermal structure of subduction zones (Leng & Mao, 2015; Syracuse et al., 2010), this large anomaly is inconsistent with the notion that because the portion of the slab near the d660 spent longer time in the mantle than that near the d410, the temperature difference between the interior of the slab and the ambient mantle should reduce and not increase with depth (e.g., Carminati et al., 2005). Therefore, subduction of anhydrous slabs may not be a feasible scenario for the observations. We emphasize that this conclusion was drawn based on estimations using a certain chosen values of Clapeyron slopes and other physical parameters. Given the large uncertainties in these parameters, the possibility that the undulations of the discontinuities are associated with subduction of anhydrous slabs cannot be totally excluded.

4.2.2. Subduction and Dehydration of Hydrous Slabs

It has long been recognized that wadsleyite and ringwoodite in the upper and lower MTZ, respectively, can incorporate a maximum of ∼3.3 wt.% of water for wadsleyite (Inoue et al., 2010; Smyth, 1987) and ∼1.7 wt.% of water for ringwoodite (Inoue et al., 2010) in their structures. Numerous mineral physics experiments (see a review by Ohtani & Litasov, 2006 for details) conclude that addition of water in the MTZ can cause the uplift of the d410 and depression of the d660. For instance, Litasov et al. (2005) find that the incorporation of 2 wt.% of water in hydrous peridotite at a temperature of 1473 K (which is lower than the normal mantle temperature at 660 km but is typical for recently subducted slabs) can result in an uplift of 15–30 km for the d410 and a 15 km depression of the d660.

As detailed below, a model with a hydrous lower MTZ can explain the observed depths for both the d410 and d660 (Figure 11b). We propose that relative to the upper MTZ, the lower MTZ is more hydrous beneath southern Sumatra, for several reasons.

(1) Addition of water tends to broaden the d410 (Smyth & Frost, 2002) more significantly than the d660 (Higo et al., 2001), which would cause a stronger P_ds from the d660 relative to the d410. Such a difference is not observed (Figures 4 and 5). Additionally, because a broader discontinuity results in weaker P-to-S conversions for higher frequencies (van der Meijde et al., 2003), we measure the frequency dependence of the d410 and d660 amplitudes for several bins that are sampled by a high number of RFs in Regions C and D. The RFs are band-pass filtered using a fixed lower frequency limit of 0.02 Hz and a varying higher frequency limit. As shown in Figure S6, the amplitude of the d660 generally decreases with higher frequencies, and that of the d410 is relatively stable. This observation is consistent with the hypothesis that the lower MTZ is hydrated, and that the water content is normal in the vicinity of the d410.

(2) Because olivine above the d410 has a much smaller water capacity than wadsleyite below the d410 (e.g., Inoue et al., 2010; Ohtani & Litasov, 2006), it has been proposed that water in the upper MTZ might migrate upward, forming a dense but low velocity layer above the d410 (Bercovici & Karato, 2003) and producing strong negative arrivals atop the d410 (e.g., Schmandt et al., 2011; Tauzin et al., 2010). The anticipated negative arrivals atop the d410 are not unambiguously observed (Figure 4).

(3) The observed uplift of the d410 can entirely be accounted for by the velocity and thermal effects associated with an anhydrous slab, as argued above. Therefore, an anomalously large amount of water is unlikely in the vicinity of the upper MTZ.

We next estimate if the addition of a certain amount of water in the lower MTZ can indeed explain the observed apparent depression of the d660. We consider four factors to be the main contributors to the observed 17 km depression of the d660, which is resultant from adding the 6 km depression from correcting the apparent uplift caused by upper mantle positive velocity anomalies and the observed 11 km depression (Figure 7b). The first factor is the negative temperature anomaly associated with the slabs. If we assume that the anomaly is the same as what was calculated using the uplift of the d410, that is, −120 K, the corresponding depression of the d660 is 4 km (assuming a Clapeyron slope of −1.3 MPa/K).

The second factor is the higher-than-normal velocity associated with the low temperature. If the scaling relationship of $dV_p/dT = -4.8 \times 10^{-4}\,\text{km s}^{-1}\,K^{-1}$ (Deal et al., 1999) is used, the estimated V_p anomaly corresponding to a −120 K thermal anomaly is 0.058 km/s (or about 0.68%). The high velocity anomaly leads to an apparent uplift of about 6 km if we assume that the entire MTZ is affected by the low temperature.

The third is the addition of water in the lower MTZ. A 1.0 wt.% of water leads to an ~8 km depression of the d660 (Litasov et al., 2005). Note that since ringwoodite has a maximum water capacity of about 1.7 wt.% (Inoue et al., 2010), a 1.0 wt.% corresponds to a 60% water storage capacity.

The fourth factor is the velocity reduction associated with the addition of water. As suggested by a recent modeling study (Figure 7 in Wang et al., 2018), adding 60% water storage capacity to $(\text{Mg,Fe})_2\text{SiO}_4$ polymorphs can decrease V_s by 0.15 km/s (about −3% anomaly) in the MTZ. Using a $\text{dln}(V_s)/\text{dln}(V_p)$ value of 2.0 and assuming that the low velocities are limited in the 140 km thick lower MTZ, the apparent depression of the d660 associated with the LVZ is about 8 km.

The net depression combining the contributions from the above four factors is 14 km (Figure 11b), which is comparable with the observed value. In spite of the obvious large uncertainties in the parameters used in the above estimates, it is reasonable to conclude that a hydrous MTZ is required in order to explain the observed variations in the observed depths of the MTZ discontinuities. Under the assumption of linear relationships between water content and the amount of depression of the d660 (Litasov et al., 2005), and between the amount of water and the magnitude of velocity reduction (Wang et al., 2018), the estimated thermal anomaly for Region C is about −140°, and the water content is approximately three fourths of that inferred for Region D.

4.3. A Weakly Hydrated MTZ Beneath the South China Sea

The westernmost portion of the South China Sea (Region E) is characterized by a marginally depressed d410 that is 6 km deeper than normal, a more significantly depressed d660 that is 18 km deeper than normal, and a 12 km thicker MTZ (Figure 7). For this area, some of the seismic tomography results indicate a slightly lower than normal upper mantle velocity of about −0.5% (Figures 2g and 2j; Lu et al., 2019; Obayashi et al., 2013). This anomaly alone can cause an apparent depression of both discontinuities by 6 km and thus can explain the d410 depth measurements.

The magnitude of water content can be estimated using the same approach presented in the previous section. Because of the lack of observable velocity anomaly in the MTZ in this area (middle column in Figure 2), it is reasonable to assume that the velocity increase from the low temperature due to slab subduction and velocity decrease caused by an excessive amount of hydrous minerals approximately cancel each other. Calculations similar to those presented in the previous section suggest the existence of a weakly hydrated MTZ beneath this area. Given the smaller magnitude of thickening relative to Region D (12 versus 28 km), the amount of water is probably around 0.5 wt.%.

5. Conclusions

The resulting depth variations of the d410 and d660 are consistent with the existence of significant thermal and water effects associated with the subduction of the Australian Plate beneath the Sunda Plate. The uplifting of the d410 in southern Sumatra and adjacent areas could be adequately explained by the low temperature anomaly induced by the subducted Australian Plate that has reached at least the d660, while the depression of the d660 is probably caused by a combination of the low temperature anomaly and the presence of water in the lower MTZ from dehydration of the subducted slab. The abnormally thin MTZ to the southwest of the Toba Caldera supports the presence of a low velocity zone in the upper mantle and the uppermost MTZ, as the result of advective thermal upwelling through a slab window.

Data Availability Statement

Data used in this study were requested from the IRIS DMC (http://ds.iris.edu/ds;last accessed: September 2018), and GEOFON (https://doi.org/10.14470/TR560404; last accessed: August 2018).

References

Akaogi, M., Ito, E., & Navrotsky, A. (1989). Olivine-modified spinel-spinel transitions in the system Mg_2SiO_4-Fe_2SiO_4: Calorimetric measurements, thermochemical calculation, and geophysical applications. *Journal of Geophysical Research*, *94*, 15,671–15,685. https://doi.org/10.1029/JB094iB11p15671

Amaru, M. L. (2007). Global travel time tomography with 3-D reference models (Ph.D. thesis), Utrecht University, the Netherlands.

Ammon, C. J. (1991). The isolation of receiver effects from teleseismic *P* waveforms. *Bulletin of the Seismological Society of America*, *81*, 2504–2510.

Anderson, D. L. (1967). Phase changes in the upper mantle. *Science*, *157*, 1165–1173. https://doi.org/10.1126/science.157.3793.1165

Argus, D. F., Gordon, R. G., & DeMets, C. (2011). Geologically current motion of 56 plates relative to the no-net-rotation reference frame. *Geochemistry, Geophysics, Geosystem*, *12*, Q11001. https://doi.org/10.1029/2011GC003751

Bercovici, D., & Karato, S. (2003). Whole-mantle convection and the transition-zone water filter. *Nature*, *425*, 39–44. https://doi.org/10.1038/nature01918

Bina, C. R., & Helffrich, G. (1994). Phase transition Clapeyron slopes and transition zone seismic discontinuity topography. *Journal of Geophysical Research*, *99*, 15,853–15,860. https://doi.org/10.1029/94JB00462

Carminati, E., Negredo, A. M., Valera, J. L., & Doglioni, C. (2005). Subduction-related intermediate-depth and deep seismicity in Italy: Insights from thermal and rheological modeling. *Physics of the Earth and Planetary Interiors*, *149*, 65–79. https://doi.org/10.1016/j.pepi.2004.04.006

Chesner, C. A., & Luhr, J. F. (2010). A melt inclusion study of the Toba Tuffs, Sumatra, Indonesia. *Journal of Volcanology and Geothermal Research*, *197*, 259–278. https://doi.org/10.1016/j.jvolgeores.2010.06.001

Chesner, C. A., Rose, W. I., Deino, A., Drake, R., & Westgate, J. A. (1991). Eruptive history of Earth's largest Quaternary caldera (Toba, Indonesia) clarified. *Geology*, *19*, 200–203. https://doi.org/10.1130/0091-7613(1991)019<0200:EHOESL>2.3.CO;2

Clayton, R. W., & Wiggins, R. A. (1976). Source shape estimation and deconvolution of teleseismic bodywaves. *Geophysical Journal International*, *47*, 151–177. https://doi.org/10.1111/j.1365-246X.1976.tb01267.x

Collier, J. D., Helffrich, G. R., & Wood B. J. (2001). Seismic discontinuities and subduction zones. *Physics of the Earth and Planetary Interiors*, *127*, 35–49. https://doi.org/10.1016/S0031-9201(01)00220-5

Dahm, H. H., Gao, S. S., Kong, F., & Liu, K. H. (2017). Topography of the mantle transition zone discontinuities beneath Alaska and its geodynamic implications: Constraints from receiver function stacking. *Journal of Geophysical Research*, *122*, 10,352–10,363. https://doi.org/10.1002/2017JB014604

Deal, M. M., Nolet, G., & van der Hilst, R. D. (1999). Slab temperature and thickness from seismic tomography: 1. Method and application to Tonga. *Journal of Geophysical Research*, *104*, 28,789–28,802. https://doi.org/10.1029/1999JB900255

Dueker, K. G., & Sheehan, A. F. (1998). Mantle discontinuity structure beneath the Colorado Rocky Mountains and High Plains. *Journal of Geophysical Research*, *103*, 7153–7169. https://doi.org/10.1029/97JB03509

Efron, B., & Tibshirani, R. (1986). Bootstrap methods for standard errors, confidence intervals, and other measures of statistical accuracy. *Statistical Science*, *1*, 54–77. https://doi.org/10.1214/ss/1177013815

Fei, Y., Van Orman, J., Li, J., van Westrenen, W., Sanloup, C., Minarik, W., et al. (2004). Experimentally determined postspinel transformation boundary in Mg_2SiO_4 using MgO as an internal pressure standard and its geophysical implications. *Journal of Geophysical Research*, *109*, B02305. https://doi.org/10.1029/2003JB002562

Foulger, G. R., Panza, G. F., Artemieva, I. M., Bastow, I. D., Cammarano, F., Doglioni, C., et al. (2015). What lies deep in the mantle below? *Eos*, *96*, 1–7. https://doi.org/10.1029/2015EO034319

Foulger, G. R., Panza, G. F., Artemieva, I. M., Bastow, I. D., Cammarano, F., Evans, J. R., et al. (2014). Caveats on tomographic images. *Terra Nova*, *25*, 259–281. https://doi.org/10.1111/ter.12041

Gao, S. S., & Liu, K. H. (2014a). Imaging mantle discontinuities using multiply-reflected *P*-to-*S*onversions. *Earth and Planetary Science Letters*, *402*, 99–106. https://doi.org/10.1016/j.epsl.2013.08.025

Gao, S. S., & Liu, K. H. (2014b). Mantle transition zone discontinuities beneath the contiguous United States. *Journal of Geophysical Research*, *119*, 6452–6468. https://doi.org/10.1002/2014JB011253

Gudmundsson, O., & Sambridge, M. (1998). A regionalized upper mantle (RUM) seismic model. *Journal of Geophysical Research*, *103*, 7121–7136. https://doi.org/10.1029/97JB02488

Hall, R., & Spakman, W. (2015). Mantle structure and tectonic history of SE Asia. *Tectonophysics*, *658*, 14–45. https://doi.org/10.1016/j.tecto.2015.07.003

Helffrich, G. (2000). Topography of the transition zone seismic discontinuities. *Reviews of Geophysics*, *38*, 141–158. https://doi.org/10.1029/1999RG000060

Higo, Y., Inoue, T., Irifune, T., & Yurimoto, H. (2001). Effect of water on the spinel-postspinel transformation in Mg₂SiO₄. *Geophysical Research Letters*, *28*, 3505–3508. https://doi.org/10.1029/2001GL013194

Hirose, K. (2002). Phase transitions in pyrolitic mantle around 670-km depth: Implications for upwelling of plumes from the lower mantle. *Journal of Geophysical Research*, *107*, 2078. https://doi.org/10.1029/2001JB000597

Huang, Z., Zhao, D., & Wang, L. (2015). *P* wave tomography and anisotropy beneath Southeast Asia: Insight into mantle dynamics. *Journal of Geophysical Research*, *120*, 5154–5174. https://doi.org/10.1002/2015JB012098

Inoue, T., Wada, T., Sasaki, R., & Yurimoto, H. (2010). Water partitioning in the Earth's mantle. *Physics of the Earth and Planetary Interiors*, *183*, 245–251. https://doi.org/10.1016/j.pepi.2010.08.003

Ito, E., & Katsura, T. (1989). A temperature profile of the mantle transition zone. *Geophysical Research Letters*, *16*, 425–428. https://doi.org/10.1029/GL016i005p00425

Jaxybulatov, K., Shapiro, N. M., Koulakov, I., Mordret, A., Landes, M., & Sens-Schonfelder, C. (2014). A large magmatic sill complex beneath the Toba caldera. *Science*, *346*, 617–619. https://doi.org/10.1126/science.1258582

Katsura, T., Yamada, H., Nishikawa, O., Song, M., Kubo, A., Shinmei, T., et al. (2004). Olivine-wadsleyite transition in the system (Mg,Fe)₂SiO₄. *Journal of Geophysical Research*, *109*, B02209. https://doi.org/10.1029/2003JB002438

Kennett, B. L. N., & Engdahl, E. R. (1991). Traveltimes for global earthquake location and phase identification. *Geophysical Journal International*, *105*, 429–465. https://doi.org/10.1111/j.1365-246X.1991.tb06724.x

Kennett, B. L. N., Engdahl, E. R., & Buland, R. (1995). Constraints on seismic velocities in the Earth from traveltimes. *Geophysical Journal International*, *122*, 108–124. https://doi.org/10.1111/j.1365-246X.1995.tb03540.x

Kong, F., Gao, S. S., Liu, K. H., Zhang, J., & Li, J. (2020). Seismic anisotropy and mantle flow in the Sumatra subduction zone constrained by shear wave splitting and receiver function analyses. *Geochemistry, Geophysics, Geosystems*, *21*, e2019GC008766. https://doi.org/10.1029/2019GC008766

Koulakov, I., Kasatkina, E., Shapiro, N. M., Jaupart, C., Vasilevsky, A., EI Khrepy, S., et al. (2016). The feeder system of the Toba supervolcano from the slab to the shallow reservoir. *Nature Communications*, *7*, 12228. https://doi.org/10.1038/ncomms12228

Lange, D., Tilmann, F., Rietbrock, A., Collings, R., Natawidjaja, D. H., Suwargadi, B. W., et al. (2010). The fine structure of the subducted Investigator Fracture Zone in western Sumatra as seen by local seismicity. *Earth and Planetary Science Letters*, *298*, 47–56. https://doi.org/10.1016/j.epsl.2010.07.020

Lawrence, J. F., & Shearer, P. M. (2006). A global study of transition zone thickness using receiver functions. *Journal of Geophysical Research*, *111*, B06307. https://doi.org/10.1029/2005JB003973

Leng, W., & Mao, W. (2015). Geodynamic modeling of thermal structure of subduction zones. *Science China: Earth Sciences*, *58*, 1070–1083. https://doi.org/10.1007/s11430-015-5107-5

Li, X., Hao, T., & Li, Z. (2018). Upper mantle structure and geodynamics of the Sumatra subduction zone from 3-D teleseismic *P*-wave tomography. *Journal of Asian Earth Sciences*, *161*, 25–34. https://doi.org/10.1016/j.jseaes.2018.05.004

Li, C., van der Hilst, R. D., Engdahl, E. R., & Burdick, S. (2008). A new global model for *P* wave speed variations in Earth's mantle. *Geochemistry, Geophysics, Geosystems*, *9*, Q05018. https://doi.org/10.1029/2007GC001806

Litasov, K. D., Ohtani, E., Sano, A., Suzuki, A., & Funakoshi, K. (2005). Wet subduction versus cold subduction. *Geophysical Research Letters*, *32*, L13312. https://doi.org/10.1029/2005GL022921

Liu, K. H., & Gao, S. S. (2010). Spatial variations of crustal characteristics beneath the Hoggar swell, Algeria, revealed by systematic analyses of receiver functions from a single seismic station. *Geochemistry, Geophysics, Geosystem*, *11*. https://doi.org/10.1029/2010GC003091

Liu, K. H., Gao, S. S., Silver, P. G., & Zhang Y. (2003). Mantle layering across central South America. *Journal of Geophysical Research*, *108*, 2510. https://doi.org/10.1029/2002JB002208

Liu, S., Suardi, I., Yang, D., Wei, S., & Tong, P. (2018). Teleseismic traveltime tomography of northern Sumatra. *Geophysical Research Letters*, *45*, 13,231–13,239. https://doi.org/10.1029/2018GL078610

Lu, C., Grand, S. P., Lai, H., & Garnero, E. J. (2019). TX2019slab: A new *P* and *S* tomography model incorporating subducting slabs. *Journal of Geophysical Research*, *124*, 11,549–11,567. https://doi.org/10.1029/2019JB017448

Mohamed, A. A., Gao, S. S., Elsheikh, A. A., Liu, K. H., Yu, Y., & Fat-Helbary, R. E. (2014). Seismic imaging of mantle transition zone discontinuities beneath the northern Red Sea and adjacent areas. *Geophysical Journal International*, *199*, 648–657. https://doi.org/10.1093/gji/ggu284

Muller, R. D., Roest, W. R., Royer, J., Gahagan, L. M., & Sclater, J. G. (1997). Digital isochrons of the world's ocean floor. *Journal of Geophysical Research*, *102*, 3211–3214. https://doi.org/10.1029/96JB01781

Obayashi, M., Yoshimitsu, J., Nolet, G., Fukao, Y., Shiobara, H., Sugioka, H., et al. (2013). Finite frequency whole mantle *P* wave tomography: Improvement of subducted slab images. *Geophysical Research Letters*, *40*, 5652–5657. https://doi.org/10.1002/2013GL057401

Ohtani, E., & Litasov, K. D. (2006). The effect of water on mantle phase transitions. *Reviews in Mineralogy and Geochemistry*, *62*, 397–420. https://doi.org/10.2138/rmg.2006.62.17

Page, B. G. N., Bennett, J. D., Cameron, N. R., Bridge, D. McC., Jeffery, D. H., Keats, W., & Thaib, J. (1979). A review of the main structural and magmatic features of northern Sumatra. *Journal of the Geological Society*, *136*, 569–579. https://doi.org/10.1144/gsjgs.136.5.0569

Pesicek, J. D., Thurber, C. H., Widiyantoro, S., Zhang, H., DeShon, H. R., & Engdahl, E. R. (2010). Sharpening the tomographic image of the subducting slab below Sumatra, the Andaman Islands and Burma. *Geophysical Journal International*, *182*, 433–453. https://doi.org/10.1111/j.1365-246X.2010.04630.x

Rampino, M. R., & Self, S. (1992). Volcanic winter and accelerated glaciation following the Toba super-eruption. *Nature*, *359*, 50–52. https://doi.org/10.1038/359050a0

Ringwood, A. E. (1975). *Composition and petrology of the Earth's mantle*. New York: McGraw-Hill.

Saita, T., Suetsugu, D., Ohtaki, T., Takenaka, H., Kanjo, K., & Purwana, I. (2002). Transition zone thickness beneath Indonesia as inferred using the receiver function method for data from the JISNET regional broadband seismic network. *Geophysical Research Letters*, *29*, 1115. https://doi.org/10.1029/2001GL013629

Schmandt, B., Dueker, K. G., Hansen, S. M., Jasbinsek, J. J., & Zhang, Z. (2011). A sporadic low-velocity layer atop the western U.S. mantle transition zone and short-wavelength variations in transition zone discontinuities. *Geochemistry, Geophysics, Geosystems*, *12*, Q08014. https://doi.org/10.1029/2011GC003668

Schulze, K., Marquardt, H., Kawazoe, T., Ballaran, T. B., McCammon, C., Koch-Müller, M., et al. (2018). Seismically invisible water in Earth's transition zone? *Earth and Planetary Science Letters*, *498*, 9–16. https://doi.org/10.1016/j.epsl.2018.06.021

Shearer, P. M., & Masters, T. G. (1992). Global mapping of topography on the 660-km discontinuity. *Nature*, *355*, 791–796. https://doi.org/10.1038/355791a0

Simons, W. J. F., Socquet, A., Vigny, C., Ambrosius, B. A. C., Haji Abu, S., Promthong, C., et al. (2007). A decade of GPS in Southeast Asia: Resolving Sundaland motion and boundaries. *Journal of Geophysical Research*, *112*, B06420. https://doi.org/10.1029/2005JB003868

Smith, W. H. F., & Wessel, P. (1990). Gridding with continuous curvature splines in tension. *Geophysics*, *55*, 293–305. https://doi.org/10.1190/1.1442837

Smyth, J. R. (1987). β-Mg$_2$SiO$_4$: A potential host for water in the mantle? *American Mineralogist*, *72*, 1051–1055.

Smyth, J. R., & Frost, D. J. (2002). The effect of water on the 410-km discontinuity: An experimental study. *Geophysical Research Letters*, *29*, 1485. https://doi.org/10.1029/2001GL014418

Stein, S., & Okal, E. A. (2005). Speed and size of the Sumatra earthquake. *Nature*, *434*, 581–582. https://doi.org/10.1038/434581a

Sun, M., Fu, X., Liu, K. H., & Gao, S. S. (2018). Absence of thermal influence from the African Superswell and cratonic keels on the mantle transition zone beneath southern Africa: Evidence from receiver function imaging. *Earth and Planetary Science Letters*, *503*, 108–117. https://doi.org/10.1016/j.epsl.2018.09.012

Sun, M., Gao, S. S., Liu, K. H., & Fu, X. (2020). Upper mantle and mantle transition zone thermal and water content anomalies beneath NE Asia: Constraints from receiver function imaging of the 410 and 660 km discontinuities. *Earth and Planetary Science Letters*, *532*, 116040. https://doi.org/10.1016/j.epsl.2019.116040

Syracuse, E. M., van Keken, P. E., & Abers, G. A. (2010). The global range of subduction zone thermal models. *Physics of the Earth and Planetary Interiors*, *183*, 73–90. https://doi.org/10.1016/j.pepi.2010.02.004

Tauzin, B., Debayle, E., & Wittlinger, G. (2010). Seismic evidence for a global low-velocity layer within the Earth's upper mantle. *Nature Geoscience*, *3*, 718–721. https://doi.org/10.1038/ngeo969

Thio, V., Cobden, L., & Trampert, J. (2016). Seismic signature of a hydrous mantle transition zone. *Physics of the Earth and Planetary Interiors*, *250*, 46–63. https://doi.org/10.1016/j.pepi.2015.11.005

van der Meijde, M., Marone, F., Giardini, D., & van der Lee, S. (2003). Seismic evidence for water deep in Earth's upper mantle. *Science*, *300*, 1556–1558. https://doi.org/10.1126/science.1083636

Wang, F., Barklage, M., Lou, X., van der Lee, S., Bina, C. R., & Jacobsen, S. D. (2018). HyMaTZ: A Python program for modeling seismic velocities in hydrous regions of the mantle transition zone. *Geochemistry, Geophysics, Geosystems*, *19*, 2308–2324. https://doi.org/10.1029/2018GC007464

Yamazaki, D., & Karato, S. (2001). Some mineral physics constraints on the rheology and geothermal structure of Earth's lower mantle. *American Mineralogist*, *86*, 385–391. https://doi.org/10.2138/am-2001-0401

Yu, Y., Gao, S. S., Liu, K. H., Yang, T., Xue, M., & Le, K. P. (2017). Mantle transition zone discontinuities beneath the Indochina Peninsula: Implications for slab subduction and mantle upwelling. *Geophysical Research Letters*, *44*, 7159–7167. https://doi.org/10.1002/2017GL073528